

NJC

Accepted Manuscript



This is an *Accepted Manuscript*, which has been through the Royal Society of Chemistry peer review process and has been accepted for publication.

Accepted Manuscripts are published online shortly after acceptance, before technical editing, formatting and proof reading. Using this free service, authors can make their results available to the community, in citable form, before we publish the edited article. We will replace this *Accepted Manuscript* with the edited and formatted *Advance Article* as soon as it is available.

You can find more information about *Accepted Manuscripts* in the [Information for Authors](#).

Please note that technical editing may introduce minor changes to the text and/or graphics, which may alter content. The journal's standard [Terms & Conditions](#) and the [Ethical guidelines](#) still apply. In no event shall the Royal Society of Chemistry be held responsible for any errors or omissions in this *Accepted Manuscript* or any consequences arising from the use of any information it contains.

Influence of precursors on phase evolution of nano iron oxide/oxyhydroxides: optical and magnetic properties

K. Rout^{*1}, M. Mohapatra^{**1}, S. Layek², A. Dash¹, H. C. Verma², S. Anand¹

¹Institute of Minerals and Materials Technology, Bhubaneswar 751013, Odisha, India

²Department of Physics, Indian Institute of Technology, Kanpur 208016, UP, India

ABSTRACT

The present investigations describe the evolution of nano iron oxides/oxyhydroxides phases synthesized under identical conditions of precipitation using different starting reagents. Depending on Fe(III) source and neutralizing agent, formation of single-phased nano goethite, single-phased ferrihydrite and a combination of goethite, hematite and ferrihydrite phases were evolved in the synthesized samples. The prepared precursors were annealed at 400, 600 and 800 °C to study the changes in morphology, optical and magnetic properties of single phase α -Fe₂O₃. Detailed characterization studies of the precursors and hematite obtained by annealing the samples were carried out using X-ray diffraction (XRD), Transmission electron microscopy (TEM), Raman and Mossbauer spectroscopy. Raman spectra of α -Fe₂O₃ obtained on annealing the precursors showed changes in peaks' positions and intensities. These changes have been attributed to surface defects, phonon confinement effect, particle shape, and surface morphology. TEM images of the as synthesized and annealed samples clearly showed difference in shape, size and crystallinity. The direct and indirect band gap energies for annealed samples estimated from UV-vis absorption spectra showed these values to be smaller as compared to bulk value for α -Fe₂O₃. The band gaps were not much affected by the nature of precursor for the formation of α -Fe₂O₃ but did depend on annealing temperature. Very interesting trends were observed for the magnetic behaviour of α -Fe₂O₃. The coercivity values varied in the range of 28.7 to 2966 Oe. Probable mechanisms of formation of different phases have been outlined.

KEYWORDS: Nano iron oxides, TEM, Mössbauer, VSM, Raman spectra, annealing

* Corresponding author: Mail ID: rrl.kalyani@gmail.com

1. Introduction

One of the most active areas of research in materials science during the last few years is related to nanosized iron oxides¹ having diameters in the range of 1 to 100 nm. Comprehensive reviews on applications and synthesis of nano structured iron oxides/hydroxides have been recently published.^{2,3} Various applications of iron oxide nano materials (NMs) are in the field of catalysis, sensors, pigments, adsorbents, enzyme supports, ferrofluids and magnetic materials.⁴⁻¹⁴ The synthesis routes include hydrothermal, sol-gel, solvothermal, mechanochemical, co-precipitation-annealing, thermal decomposition, microwave plasma, micro emulsion and surfactant mediation etc.¹⁵⁻¹⁸ The experimental parameters for synthesis of nano iron oxides play a key role in determining the size distribution, morphology, magnetic properties and surface chemistry.⁵ Some of the recent works^[1, 19-37] on synthesis are summarised in Table S₁. Uniformly distributed nano particles of ferrihydrite and goethite can be obtained through single stage precipitation methods. In case of nano hematite particles, hydrothermal, solvothermal or precipitation-annealing methods are employed. Though through hydrothermal synthesis hematite particles with tuneable size and morphology can be obtained but the process suffers from three main drawbacks namely, (i) expensive equipment, (ii) high maintenance costs, and (iii) low inputs in term of iron content. In case of solvothermal synthesis an additional cost of solvent and its removal from the final product has to be incurred. Therefore, precipitation of precursor followed by annealing still remains to be a much sought after route for synthesizing hematite.

Though a great deal of literature is available on iron oxides/hydroxides prepared under different experimental conditions, yet no work has been devoted to outline the effects of starting reagents on formation of nano iron oxides/oxyhydroxide phases synthesized under identical precipitation conditions in terms of concentration of reagents, pH, time, temperature and ageing. The main objective of the present work is to investigate the reagent dependence phase evolution of nano iron oxide/hydroxides formed in such reactions. Another goal of this study is to compare structural, optical and magnetic properties of nano α -Fe₂O₃ particles obtained by annealing the as synthesized precursors having different phases of iron oxides/hydroxides. To the best of our knowledge such an exhaustive comparative study has not been presented earlier.

2. Experimental

2.1 Materials

$\text{Fe}(\text{NO}_3)_3 \cdot 9\text{H}_2\text{O}$, sodium hydroxide and ammonia used for synthesis were obtained from E-Merck, India. Iron citrate was from ACROS organics.

2.2. Synthesis Procedure

1M stock solutions of ferric nitrate and ferric citrate were prepared. 10 M stock solutions of neutralizing agents i.e., ammonia and sodium hydroxide were prepared. The synthesis was carried out at room temperature by taking 100 mL of 1M Fe(III) solution and adjusting the pH to 12 by slow addition (20 drops /min) of 10 M ammonia/sodium hydroxide. The resulting suspension was placed into 2.5 L acid resistive plastic bottles and aged at 60 °C for 24 h. The suspension was filtered and washed with water until the filtrate was free of nitrate and alkali. The samples so obtained were dried for 24 h at 100 °C in an air oven. Coding of four samples synthesized with different combinations of iron source and precipitating agents are given in Table 1.

2.3. Characterization

Iron was analyzed volumetrically.³⁸ The X-ray diffraction (XRD) measurements for the as prepared samples were done over a range of 5 to 40° using a Phillips Powder Diffractometer Model PW1830 with $\text{MoK}\alpha$ radiation at a scan speed of 1.2° min⁻¹. The room temperature XRD patterns for all annealed samples were taken over a 2 θ range of 30 to 110° using Seifert Iso-Debyeflex 2002 Diffractometer with $\text{Cr-K}\alpha$ radiation at a scan speed of 1° per min. Raman spectra of as prepared and annealed samples were taken using a Renishaw (Renishaw plc, Gloucestershire, U.K.) instrument via micro Raman spectrometer equipped with a 514 nm green laser having a 1 cm⁻¹ spectral resolution of the Raman shift, an X-Y step resolution of 0.1 μm , and a confocal resolution of 2.5 μm . The surface morphologies of the samples were studied using an electron microscope (FEI, TECNAI G2 20, TWIN) operating at 200 kV, equipped with a GATAN CCD camera. UV-Vis spectra of the synthesized and annealed samples were measured using an UV-Vis Perkin Elmer Lambda 35 model. Deionised (DI) water in a UV-Vis quartz cell was used as the blank. Mössbauer spectra of the samples were recorded at room temperature using a standard constant acceleration Mössbauer spectrometer in the transmission geometry. A 25 mCi ⁵⁷Co embedded in a Rh-matrix was used as the radioactive Mössbauer source during the experiment. The collected experimental data have been fitted with a least-squares computer based program by considering the Lorentzian line shape of the spectrum. All the parameters have been calculated by taking the Mössbauer

spectrum of bcc iron as the calibration. Room temperature magnetization was measured for all the samples as a function of applied magnetic field (hysteresis loops) using a vibrating sample magnetometer (VSM, ADE Technologies, USA) up to highest applied field of 1.5 Tesla (T). The sensitivity of the VSM instrument is quoted to be 10^{-6} emu. The measurements of the mass for the VSM studies were done with an electronic balance having sensitivity of 0.1 mg. The experimental error in measuring magnetization is around 10^{-4} emu/g.

3. Result and Discussion

3.1. Characterization of As Synthesized and Annealed K_1 , K_2 , K_3 and K_4 samples

The detailed characterization studies were carried out on as synthesized as well as annealed samples. The results are presented in the following subsections.

3.1.1 XRD Studies. The XRD patterns of the as synthesized samples are shown in Figure 1. The XRD pattern of K_1 sample shows characteristic peaks at 2θ values of 21.5, 33.5, 36.9, 41.4, 53.5, 59.3° corresponding to the (110), (130), (111), and (210), (131), (211) planes of goethite (JCPDS file card, no. 03-0249). In case of sample K_2 , the peaks at 2θ values of 15, 22.1 and 31.3° correspond to the (104), (024) and (119) planes of hematite (JCPDS file card, no. 33-0664) whereas the peaks at 2θ values of 16.1, 18.4, 24.1, and 27.5° correspond to the (110), (112), (114), and (115) planes of the ferrihydrite (JCPDS card no. 29-0712). A low intensity peak at 2θ value of 9.6° corresponds to (020) plane of goethite. It is clear that the sample is a mixture of ferrihydrite, goethite, and hematite, with major phase as ferrihydrite. The XRD pattern of the sample K_3 shows a broad spectrum with ferrihydrite as the only phase. The sample K_4 shows planes corresponding to ferrihydrite, hematite and goethite with 6-line ferrihydrite as the major phase. From the XRD patterns, it is observed that when the iron source is ferric nitrate and the neutralising agent is changed from NaOH to NH_3 (for K_1 and K_2) the phase formation changes from goethite to mixed phases of ferrihydrite, hematite and goethite. Similarly when the iron source is iron citrate and the neutralising agent is changed (for K_3 and K_4) the phase formation changes from ferrihydrite to mixed phases of ferrihydrite, goethite and hematite. Since all the preparation conditions were kept same, the observed differences in crystalline phases are only due to difference in starting materials.

The XRD patterns of K_1 , K_2 , K_3 and K_4 annealed samples are presented in Figures 2 (a) to 2 (c). All the peaks of 400°C annealed samples (Figure 2 (a)), indexed as (012), (104), (110), (113), (024), (116), (122), (214), and (300) can be assigned to the rhombohedral structure with space group $R\bar{3}c$ which is same as that of a pure bulk hematite sample. No other peaks

from any phases can be detected at least to the detection limit of the X-ray diffractometer used. Combination of ferrihydrite, goethite and hematite phases were observed in the XRD patterns of the as-prepared samples K_2 and K_4 . Complete conversion of the mixed ferrihydrite, goethite and hematite phases into pure hematite phase is seen to occur by annealing the samples at 400 °C. Similarly K_1 and K_3 samples which were goethite and ferrihydrite to start with, have completely converted to hematite. However, the full width at half maximum (FWHM) of the peaks are quite different for the four samples showing the effect of starting materials. The further increase in the annealing temperature from 400 to 600 and 800 °C leads to increase in peak intensities (shown in Figures 2(b) and (c)) without changing the crystal structure as expected. The increase in the peak intensities is a signature of increase in the crystallinity and increase in the crystallite size. The mean crystallite diameter (MCD) for each annealed sample is calculated from Scherrer formula by using FWHM of (104) (116), and (300) peaks after correcting for instrumental broadening and then averaging these three values. These planes were selected as for most of the samples these planes had more % relative intensities.

The MCD values of all the samples annealed at three different temperatures and lattice parameters are given in Table S₂. The values show that the grain growth process sharply depends on the starting material. For 400 °C annealed samples, the as-prepared samples had very different compositions as K_1 was almost exclusively goethite while K_3 was exclusively ferrihydrite. At 400 °C, these converted to 16 and 9 nm crystallites of hematite. On the other hand the mixed phases show conversion to bigger crystallites on annealing, averaging at 22 nm for K_2 and 35 nm for K_4 , Ferrihydrite seems to show slowest grain growth. In the mixed phases, already hematite nucleation had started. On annealing at higher temperatures the MCD values of all the samples increased but for K_3 it still retained the lowest size.

3.1.2 Mössbauer Studies. Room temperature Mössbauer spectra of the four as-prepared samples are shown in Figure 3 and the parameters extracted from the least square fit are presented in Table S₃. The black dots and the solid blue line represent the experimental data points and least square fit of the spectrum respectively. It is observed that the black dots match well with the solid blue line suggesting good fit of each spectrum. The Mössbauer spectrum for the as-prepared sample (shown in Figure 3 (a)) of K_1 can be fitted with two magnetic sextets corresponding to the isomer shift (IS) ≈ 0.35 mm sec⁻¹, quadruple splitting (QS) ≈ -0.23 mm sec⁻¹ and hyperfine field (B_{HF}) ≈ 34.3 and 37.8 respectively. All the

Mössbauer parameters of these two sextets match well with goethite (α -FeOOH) phase.²⁹ So, the Mössbauer spectroscopy confirms that the as-prepared sample of K₁ is pure goethite which is observed from the XRD results discussed above.

The Mössbauer spectrum of as-prepared K₂ sample (shown in Figure 3 (b)) can be best fitted with a single doublet and three sextets. The doublet corresponding to isomer shift \approx 0.30 mm/s and quadruple splitting \approx 0.67 mm sec⁻¹ represents ferrihydrite phase.³⁰ The sextet with IS \approx 0.36 mm/s, QS \approx -0.19 mm/sec and B_{HF} \approx 50.7 T corresponds to the hematite phase. The sextets with isomer shift in the range of \approx 0.34-0.38 mm sec⁻¹, negative quadruple splitting, and hyperfine field in the range of \approx 33.4 -37 T are identified as goethite phase³⁹. The area ratios 66, 20 and 14 % for ferrihydrite, hematite and goethite phases respectively are observed. The Mössbauer spectrum for the as-prepared K₃ sample (shown in Figure 3 (c)) shows single doublet corresponding to isomer shift \approx 0.31 mm sec⁻¹ and quadruple splitting \approx 0.68 mm sec⁻¹ representing pure ferrihydrite phase formation⁴⁰. No signature of any sextet coming from goethite or hematite is found in the Mössbauer spectrum confirming the XRD results. The Mössbauer spectrum of as-prepared K₄ sample (Figure 3 (d)) can also be fitted with a single doublet and three sextets corresponding to ferrihydrite, hematite and goethite phases like as seen in the spectrum of K₂ sample. The area ratios of these three phases are calculated to be 40, 38 and 22 % for K₄ sample. In XRD pattern both hematite and goethite phases were not very prominent but Mössbauer spectrum clearly shows the presence of all three phases.

The Mössbauer spectra of all the four samples (K₁, K₂, K₃ and K₄) annealed at 400 are presented in Figures 4 while the Mössbauer spectra of the samples annealed at 500 and 800 °C are given in supporting Figure S₁. The parameters are presented in Table 2. The samples K₁, K₂ and K₄ show only a single sextet with B_{HF} \approx 51 T corresponding to hematite. The sample K₃ formed from iron citrate and sodium hydroxide gives three components in the Mössbauer spectrum. The most intense component is 51.2 T sextet of hematite but another sextet at 47 T of B_{HF} and a doublet with IS \approx 0.31 mm/s and QS \approx 0.72 mm sec⁻¹ also appear. The doublet (4% area) corresponds to ferrihydrite showing that the conversion to hematite is not complete at 400 °C. The sextet with 47.0 T is most likely hematite with small particle size. From the XRD, the average crystallite size is only 9 nm. The smaller particles will show a fluctuation of magnetic moment due to thermal energy reducing the effective magnetic moment in the symmetry direction giving rise to a smaller hyperfine field. The fact that the linewidth of the two sextets is not large, 0.35 mm/s and 0.37 mm/s, suggests that the hematite

particles in the 400 °C annealed samples have a binomial distribution, the larger one giving full 51.2 T of B_{HF} and the smaller one giving 47.0 T. For all the samples annealed at higher temperatures, 600 and 800 °C, only hematite peak with $B_{HF} \approx 51.2$ T is observed.

3.1.3 Raman Spectra. The Raman spectra of as prepared samples are given in Figure S₁. As expected the sample K₁ which is pure goethite shows sharp bands at 241, 297, 395, 479, 545, 674, 996 and 1326 cm^{-1} which correspond to Raman bands for different bonding frequencies of goethite. The Raman peaks appearing at 241, 297, 395 and 479 are attributed to the A_{1g} mode of Fe-O symmetric stretching, E_g Fe-OH symmetric bending, E_g Fe-O-Fe/-OH symmetric stretching and A_{1g} -Fe-OH asymmetric stretching. The Raman peaks appearing at 545, 674 cm^{-1} are related to Fe-OH asymmetric stretching and Fe-O symmetric stretching of goethite phase. Raman peak at 996 cm^{-1} also belong to goethite phase.⁴¹

The Raman spectrum of K₂ sample shows only a few bands at 221, 288, and 669 cm^{-1} corresponding to both goethite as well as ferrihydrite. The hematite bands at 402 and 491 cm^{-1} are assigned to E_g (Fe-O symmetric bending) and A_{1g} (Fe-O symmetric stretching). In the case of hematite the band at 1326 cm^{-1} can be explained as a shifted band (1306 cm^{-1}) which is due to two-magnon scattering resulting from the interaction of two magnons associated with proximate anti parallel spin sites.⁴² The Raman spectrum of K₃ sample shows the peaks at 215, 285, 390 and a broad peak around 1286 cm^{-1} which are characteristic Raman bands of iron oxy hydroxide.⁴³

Similar to K₂, the Raman spectrum of the K₄ sample also shows few sharp bands at 222, 292, and 667 cm^{-1} corresponding to goethite as well as ferrihydrite and a shoulder at 607 cm^{-1} for the ferrihydrite phase. The hematite bands at 397 and 498 cm^{-1} are assigned to E_g (Fe-O sym bend) and A_{1g} (Fe-O sym str) respectively. These results are consistent with the finding of Mossbauer, and XRD results.

The Raman spectra of series of samples (K₁ to K₄) obtained at different annealing temperatures are presented in Figures 5(a) to 5(c) and the corresponding Raman data are given in Table S₄. All the annealed samples show peaks corresponding to various Raman modes of hematite. No other peaks corresponding to hydroxide or impurities were observed. With the increase in annealing temperature the peaks shifted towards higher wave number except for the one appearing at 500 cm^{-1} (A_{1g} representing Fe-O symmetric stretching) which showed shift to the lower wave (red shift) number on annealing at 800 °C. The blue shifts can be attributed to formation of defects on the surface of hematite nano particles at high heat

treatment temperature. Oxygen vacancies within the material or disorder induced defects strongly affect the frequency shifting. Besides oxygen vacancies there are other two possible reasons: (i) a phonon confinement effect and (ii) surface strain after annealing. Xu et al. reported blue shift on coated TiO₂ and explained the peak shifts in terms of surface strain.⁴⁴ New peak appearing at 659 cm⁻¹ for K₁ and K₃ samples annealed at 800 °C could be disorder-induced breaking of symmetry properties of phonons which may also be caused by the defects.⁴⁵ These observations emphasize on crystallite growth and induction of defects (causing strain) during the heat treatment. Similar observations were made by Šćepanović et al. for the Raman spectrum of TiO₂ nano powder after heating at 900 °C confirming crystallite growth due to heating.⁴⁶ The red shift of Raman mode at 500 cm⁻¹ for the sample K₁ annealed at 800 °C may be due to the tensile residual stress on annealing.⁴⁷

The intensities of all the peaks corresponding to A_{1g}(1), E_g(2)+E_g(3), E_g(4), A_{1g}(2), E_g(5) modes either decreased with the increase in annealing temperature from 400 to 600 °C or remained same (except in case of K₁ sample wherein at 600 °C the peak intensity corresponding to E_g(2)+E_g(3) mode marginally increased). Further increase in annealing temperature to 800 °C resulted in reduction in peaks' intensities to a much larger extent (between half or to one third). With the increase in crystallite size, the peak intensities should increase due to grains growth and increase in long range symmetry.⁴⁸⁻⁵⁰ The particle size distribution, existence of different shapes of particles, type and magnitude of the strain (compressed or tensile), discrepancy from stoichiometry as well as type of defects etc. may contribute to anomalous behavior⁵¹ i.e., decrease in peaks intensities. Xie et al. showed that the decrease in the Raman intensity of bulk oxides with increasing temperature could be correlated with an increase in the optical absorbance of the sample at the frequencies involved in the Raman process.⁵² Yang et al. reported reduction of Raman scattering up to a factor of about 25 for ZnO nanostructures and related the reduction to the surface defects.⁵³ In the present study the reduction in peaks' intensities may be due to particle shape, surface morphology and surface defects. In case of peak corresponding to second harmonic vibration (1306 cm⁻¹), sample K₁ shows significant increase in peak intensity when annealed at 600 °C.

3.1.4 TEM (transmission electron microscope) Studies. TEM images and corresponding SAED (selected area electron diffraction) patterns of the four samples are given in Figures 6(a) to 6(d). Acicular type goethite particles (breadth 50 nm and length 400 nm) are observed in the TEM image of K₁ sample (Figure 6a₁) and the SAED pattern (Figure 6a₂) shows sharp

diffraction rings corresponding to (110), (111), (115), and (103) planes of goethite. The TEM image of K₂ sample (Figure 6b₁) consists of agglomerated particles around the acicular goethite particles. Here the epitaxial consists of a ferrihydrite centre without the growth of acicular goethite. In the synthesis process the only change in experimental conditions was change of neutralizing agent. Herein ammonia has restricted the formation of goethite but at the same time aided the formation of hematite. The SAED pattern (Figure 6b₂) is indexed to (110) plane of goethite, (112) and (115) planes of ferrihydrite. The (104) plane of hematite is also marked. The TEM image of sample K₃ consists of agglomerated spherical particles of 3-5 nm size as shown in Figure 6(c₁). The corresponding SAED pattern given in Figure 6(c₂) shows diffused rings matching to ferrihydrite phase.

From the TEM micrograph of sample K₄ as given in Figure 6(d₁), formation of agglomerated spherical particles along with rod shaped particles is evident. After carefully indexing the textured SAED rings given in Figure 6(d₂), it is noticed that the first intense broad ring has a contribution from the (111) peak of the (ferrihydrite) and other two corresponds to (110) plane of ferrihydrite and (020) plane of goethite. Thus starting material not only affected the phase, it also affected the morphology and agglomeration. Fe(NO₃)₃ with NaOH gives well separated goethite rods about 50 nm thick while Fe citrate with NaOH gives very fine (sub 10 nm) particles. Iron citrate gives more densely agglomerated particles.

The TEM of K₁ sample annealed at 400 °C given in Figure 7(a₁) shows that the acicular goethite has partly converted to similar shape of hematite particles as well as separate spherical/elliptical hematite as shown by arrows. Here it is very interesting to note that spherical particles try to separate from the rods as shown by arrows. The selected area electron diffraction (SAED) pattern of the sample given in Figure 7(a₂) shows clear diffraction spots, which indicates the high crystallinity of hematite nanoparticles. On further increasing the annealing temperature to 600 °C, the rod shape is not observed and the hematite particles grow as spherical and elliptical particles. The SAED pattern shows different planes of hematite. The TEM micrograph for K₁ sample annealed at 800 °C does not show much difference in shape of the particles but agglomeration to some extent is observed. XRD pattern of the K₁ samples annealed at 400 °C gives an average crystallite size of 16 nm. Comparing with TEM picture, one finds that there are multiple crystallite in many of the hematite particles.

The particle morphology of the K₂ sample prepared from iron nitrate neutralized by ammonia varies sharply with temperature at which the sample is annealed. In case of K₂

sample annealed at 400 °C shown in Figure 8 (a₁), the hematite nanoparticles appear to have a rhombohedral to near spherical shape with particle size varying from 70 nm to 150 nm. The selective area electron diffraction (SAED) pattern, depicted in Figure 8(a₂) confirmed (104), (113), (116) and (300) planes of hematite. On comparing the crystallite sizes as determined from XRD data, it can be visualized that at 400 °C, polycrystalline particles are formed (mean crystallite diameter (MCD)) 22 ± 3 nm, TEM 70 to 100 nm). Figure 8(b₁) shows that the hematite particles form long chains consisting of several nanoparticles for sample K₂ on annealing to 600 °C. The particle size varies between 30 and 60 nm. Hematite planes can be seen in the SAED pattern shown in Figure 8(b₂). XRD pattern gives a crystallite size of 49 nm. This shows that these are single crystallite particles. On further annealing sample K₂ to 800 °C, irregular shaped agglomerated particles of α -Fe₂O₃ are formed (Figure 8(c₁)). The corresponding SAED pattern is shown in Figure 8(c₂). The particles form large agglomeration though fine structure seems to be present within.

Microstructures of sample K₃ annealed at 400, 600 and 800 °C were not studied as it gave very low values of Hc (discussed in later part). TEM image of sample K₄ shows a mixture of cubic and spherical NPs of hematite as given in Figure 9(a₁). Formation of rings in the selected area electron diffraction pattern (SAED) (Figure 9(a₂)) of the sample shows hematite planes. There is not much difference in particles shape after annealing at 600 °C but the particles appear as single crystallites with no agglomeration. On annealing at 800 °C though the shape seems same but aggregation of particles is visible. For this sample, the particles are multi crystallite to start with and on heating, the crystallite in the particles itself merge to make single crystallites. The SAED pattern of K₄ samples annealed at 800 °C does not show much of a ring structure, as the particle size is 100 nm or above and so is the crystallite size. For the selected area for the SAED this will be more like a single crystal giving spot like pattern.

3.2. Optical Properties of As Prepared and Annealed Samples

Figure 10 illustrates the UV-Vis spectra of as synthesized K₁ to K₄ series of samples. The iron oxides absorb strongly in the UV region and weakly in visible/near IR region. The iron oxide UV-vis spectra results from three types of electronic transitions: (i) Fe^{III} crystal or ligand field transitions, (ii) interactions between magnetically coupled Fe^{III} ions, and (iii) oxygen- metal charge transfer excitation from O(2p) non bonding valence bond to Fe(3d) ligand field orbitals.⁵⁴ Sample K₁ which is pure goethite shows two bands near 289 nm and 368 nm corresponding to $6A_1 \rightarrow 4T_1(4P)$ charge transfer and $6A_1 \rightarrow 4E(4d)$ transition

respectively. Sample K₂ shows a band near 250 nm which can be assigned to $6T_{1u} \rightarrow 6T_{1u}$ transition of ferrihydrite. It has been reported that the band at 250 nm also corresponds to $6T_{1u} \rightarrow 6T_{1u}$ transition of goethite but here broad peak was observed. Sample K₃ shows a band around 350 nm, a saturated band below 400 nm is due to a paired $Fe^{3+} \rightarrow O^{2-}$ charge transfer, which extends to the shorter wavelength region. The broad band around 350 nm can be explained as a combination of the charge transfer and the variation of 6-fold coordination environments around the Fe.⁵⁵ Sample K₄ which is a mixture of ferrihydrite, hematite and goethite shows band at 209 nm which is assigned to $1T_{2u} \rightarrow 2t_{2g}$ transition of goethite. The red-shift in this charge transfer band may arise from shortening of the Fe-O bonds. In smaller particles, the Fe-O octahedra are compressed due to higher surface stress.²³ It is observed that in a mixture of ferrihydrite, goethite and hematite only goethite phase is identified. Scheinost et al. have also reported that in a mixture of ferrihydrite and goethite the difference in band position is too small to be recognised.⁵⁶

Generally, the Tauc Mott (TM) plot is used to determine the bandgap of semiconductor materials.⁵⁷ The relationship of absorption coefficient and the incident photon energy of semiconductors can be experimentally obtained using Tauc's formula:

$$\alpha h\nu = A (h\nu - E_g)^n$$

where α is the absorption coefficient, A is a constant, and n is equal to 2 for allowed direct transitions and 0.5 for indirect transitions. Table 3 shows the values of direct and indirect band gaps, respectively. The indirect transition has been identified as a spin-forbidden $Fe^{3+} 3d-3d$ excitation, while the direct transition corresponds to the $O^{2-} 2p-Fe^{3+} 3d$ charge transfer.⁵⁸

In case of K₁ sample the direct transition band gap agrees well with the previously reported results of goethite suggesting that nano goethite is a direct bandgap material.⁵⁹ The direct band gaps for as synthesized samples K₁, K₂, K₃ and K₄ were 2.8, 2.1, 2.65 and 1.9 eV. The reported band gap for ferrihydrite is 2.7 eV.⁶⁰ The direct band gap of sample K₃ is almost similar to the ones reported in the literature. It is observed that for the samples which have mixed phases (samples K₂ and K₄) band-gap energies decreased and the bands were blue shifted. Such a blue shift can be ascribed to quantum confinement effect. The quantum size effect results in the delocalization and quantization of the electronic state in the nanostructures, resulting in a change in the absorption.⁶¹ The indirect band gaps were 2.1, 1.7, 1.7 and 1.2 eV respectively. In all the cases the indirect band gaps are smaller than the direct

ones. If the indirect band gap results primarily from the surface atoms, the smaller indirect band gap may indicate that nanoparticles with a higher fraction of atoms residing at the surface provide enough phonons and lattice vibrations which are available to assist the indirect electron transition from the valence band to the conduction band.

The UV–vis spectra of the annealed samples looked more or less similar. A typical spectrum of K₂ sample annealed at 400 °C is shown in Figure S₂. The estimated band gaps for all the samples annealed at 400, 600 and 800 °C are given in Table 3. The band observed near 550 nm is assigned to the pair excitation processes $6A_1(6S) + A_1(6S)$ to $4T_1(4G) + 4T_1(4G)$ and is most likely overlapped by the contributions of $6A_1(6S)$ to $4E$, $4A_1(4G)$ ligand field transitions at 430 nm and the LMCT transition band tail (direct transitions). Among the various inter band transitions of hematite, the double excitation process ($6A_1(6S) + 6A_1(6S)$ to $4T_1(4G) + 4T_1(4G)$) yields the strongest absorption band at around 535 nm; thus, it is mainly responsible for the red colour of hematite.⁶² The band gaps for direct transitions for the annealed samples varied in the range of 1.2 to 1.6 eV. It means that for the annealed samples the values reduce significantly for most of the samples when compared to that of bulk hematite. Similarly the indirect band gap reduced for all the samples. Iron (III) oxide has a bandgap of 2.0 to 2.1 eV, therefore absorbing solar radiation from 600 to 295 nm.⁶³ From Table 3 it is observed that on annealing both direct and indirect band gaps decrease as compared to the as synthesized samples due to transformation of various phases to hematite. Electrons are highly localized in nano particles and the interaction between these localized states may give rise to the observed band gaps. As the temperature increases these localized states spread, modifying the band structures, resulting in reduction in band gap.⁶⁴ Also, reduction in the band gaps can be attributed to charge transfer from bulk to the surface of the nanocrystal.⁶⁵ Here, it is essential to emphasize that for all the four samples the numerical values of direct and indirect band gaps are close to each other for hematite obtained at a particular annealing temperature though these values for the precursor are quite different due to presence of different phases (single phase goethite, single phase ferrihydrite, or mixed phases of goethite, ferrihydrite and hematite). It indicates that the band gaps are not much affected by the nature of precursor for formation of α -Fe₂O₃ but do depend on annealing temperature.

3.3. Magnetic Properties of As Prepared and Annealed Samples

It has been observed that depending on the starting materials pure goethite, pure ferrihydrite or a combination of goethite, hematite and ferrihydrite phases were formed. On annealing at 400-800 °C all the samples transformed to hematite (except K₃ sample annealed at 400 °C which showed presence of small amounts of ferrihydrite along with hematite). Bulk ferrihydrite orders antiferromagnetically below 120 K with a small ferromagnetic-like moment arising from uncompensated spins present either inside or at the surface of the particles.⁶⁶ Goethite shows antiferromagnetic transition at about 400 K.⁶⁷ Hematite in bulk form undergoes two types of magnetic transition. One is at the Neel temperature⁶⁸ (T_N) of about 950 K below which it behaves like a weak ferromagnetic compound and the other one from weak ferromagnetic to antiferromagnetic transition at about 260 K known as Morin transition (T_M).⁶⁹

Room temperature magnetic hysteresis loops of all the as-prepared samples are plotted in Figure 11, measured upto the highest applied field of 1.5 Tesla (T). The values of magnetization at highest applied magnetic field (M_{1.5T}), remanent magnetization (M_r), coercive field (H_C) and squareness (S) as calculated from the VSM experiments are presented in Table 4. The magnetization for the as-prepared K₁ sample increases linearly with increasing magnetic field and does not saturate upto the highest applied magnetic field (1.5T). This kind of magnetic hysteresis loop behavior is a signature of paramagnetic or antiferromagnetic particles. K₁ sample is purely goethite with rod like particles which are antiferromagnetic at room temperature, hence the observed hysteresis loop is expected for such particles.

The magnetization loops for the K₂ and K₄ as-prepared samples (which are combination of ferrihydrite, hematite and goethite phases) look similar. The magnetization increases with increasing magnetic field upto 1.5T. A slope change in the magnetization curve can be seen at around 0.8 T. At room temperature ferrihydrite and goethite phases are in paramagnetic and antiferromagnetic states respectively. Presence of hematite particles, which are present in K₂ and K₄ sample, are expected to show a weak ferromagnetism. As a result, these two samples show higher coercive field. The magnetization curve of K₃ sample look similar to that of K₁ sample where the magnetization increases linearly with increasing field showing zero remanent magnetization and coercive field. This kind of paramagnetic like hysteresis curve is expected for ferrihydrite sample which orders anti-ferromagnetically below 120 K.⁶⁶

The magnetic properties of α -Fe₂O₃ particles greatly depend on the microstructures, crystallite sizes and interparticle interactions⁷⁰⁻⁷⁵. It has been reported that hematite

nanoparticles of particle size below 20 nm show superparamagnetism with zero remanent magnetization and coercive field.⁶⁰ The coercivity increases with the increase in the particle size for hematite particles with size above 20 nm. The shapes and characteristics of the M-H curves of hematite converted from different as-prepared samples also vary together with their particle size and morphology. Figure 12a gives the M-H curves for samples annealed at 400 °C. At this annealing temperature, all the samples have converted to hematite (except a small fraction of ferrihydrite left in K₃). But M-H curves of K₂, K₄ annealed at 400 °C are quite different from those of samples K₁ and K₃ annealed at 400 °C. Both K₂ and K₄ samples annealed at this temperature are well grown nearly spherical particles of hematite as can be seen from the TEM pictures (Figures 8-9). In M-H curve these samples show hysteresis loop, typical of weak ferromagnetic system with coercive fields of 1917 Oe and 1310 Oe respectively. The sample K₁ annealed at 400 °C has particles with spherical shapes and small size together with those having acicular shape (Figure 7). The average crystallite size from the XRD is 16 nm. The acicular particles of goethite are antiferromagnetic. Possibly in the hematite particles of this shape weak ferromagnetism is too weak. The spherical particles which have come out of the acicular rod like structure are small in size and are likely to show much reduced weak ferromagnetism due to thermal fluctuation. Similarly, for the K₃ sample annealed at 400 °C, the crystallite size is 9 nm and there too the weak ferromagnetism could be suppressed. The M-H loops of K₁ and K₃ samples (annealed at 400 °C) are more like that of an antiferromagnetic material. However, a small coercive field of 138 and 29 Oe can be seen from the hysteresis loops.

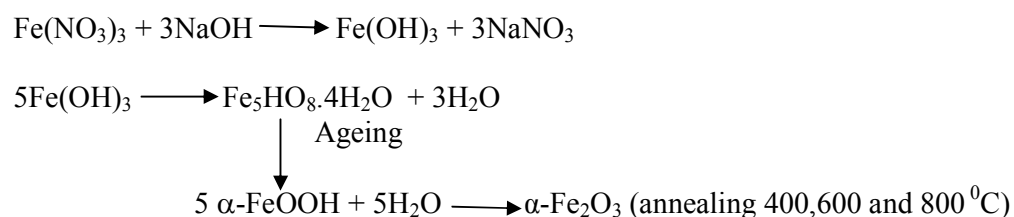
All the samples annealed at 600 °C show clear hysteresis (Figure 12b). The coercive field is lowest for K₃ but even that is 759 Oe. In all the samples, the particles are well above 50 nm in size, though the crystallite size is smaller in K₃. The maximum coercive field is 2021 Oe. The behaviour from 600 °C to 800 °C is quite different for different samples. While the coercive field for K₁, K₂ and K₄ samples increased with annealing temperature (K₂ sample showing maximum coercivity of 2966 Oe) that of K₃ steeply decreased from 759 to 307 Oe. It has been mentioned in Table S₂ that the crystallite sizes of all the samples increase with the increase of annealing temperature. In such a situation the coercivity values should show proportional increasing trend.⁷⁶ Figure 13 shows the effect of MCD on coercivity when the samples are annealed at different temperatures. It is observed that though the MCD values increase with the increase of annealing temperature, in case of sample K₂ annealed at 400 °C, the particle sizes seem much bigger in TEM images when compared to the ones obtained at

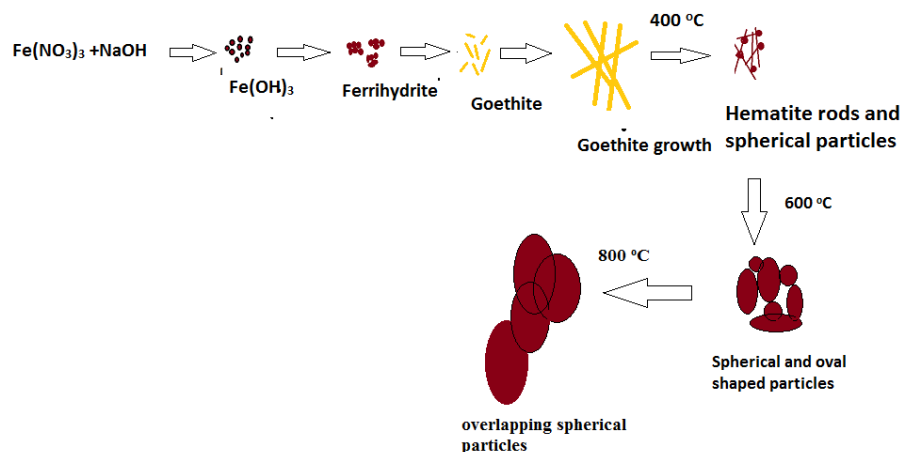
600 °C (Figure 8a and 8b) . As a corollary, the coercivity value should be higher for the 400 °C annealed K₂ sample when compared to the one obtained at 600 °C but this is not the case. The MCD values are 22 and 49 nm for K₂ sample annealed at 400 and 600 °C respectively. If the coercivity was only a function of MCD, then its value should have been much higher for the 6000 C annealed K₂ sample. The lower value of MCD as compared to observed TEM particle size suggests presence of sub particles of smaller size. Such sub particles within the crystal tend to give high coercivity values. Such anomalous trends in coercivity can be explained by (i) shape anisotropy^{22, 37} and (ii) polycrystalline nature of particles.⁷⁷ In the present studies hematite particles obtained on annealing sample K₃ (single phased ferrihydrite) went through a maxima when it was annealed at 600 °C giving a coercivity value of 759 Oe which decreased to 307 Oe for the 800 °C annealed K₃ sample though MCD values had increased with the increase of temperature (Figure 13). Vallina et al. have recently reported enhanced values of coercivity for the hematite pseudo spherical particles obtained by annealing carbonated ferrihydrite in the temperature range of 350 to 1000 °C.⁷⁶ These trends once more emphasise that the dependence between magnetic coercivity, temperature, and particle sizes still remains to be a matter of debate.

3.4. Mechanism of Phase Evolution Using Different Starting Materials

In the present study, the formation of various pure and mixed iron oxides phases is due to difference in the starting materials. We attempt to suggest mechanisms for the formation of various phase.

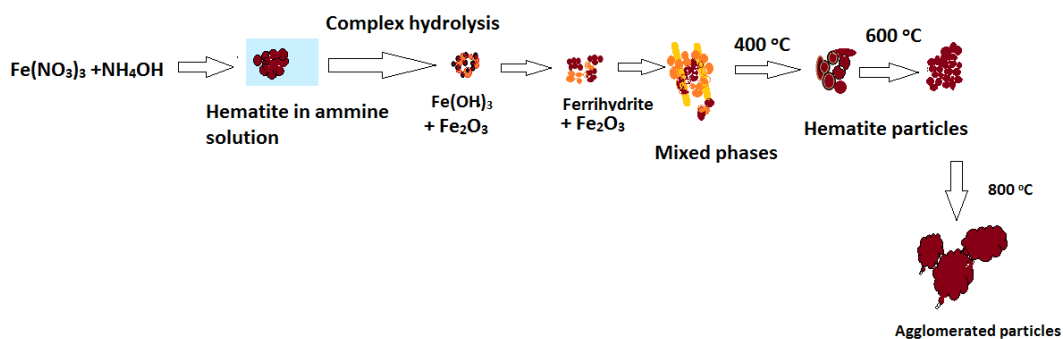
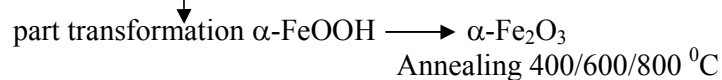
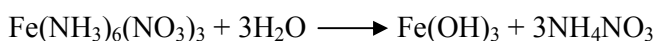
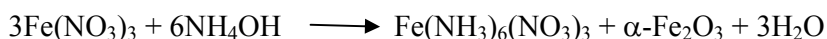
Ferric nitrate-sodium hydroxide medium (sample K₁). The probable reactions taking place during formation of goethite in ferric nitrate-sodium hydroxide medium are given below. It has been reported that first ferric hydroxide is formed which transforms to ferrihydrite prior to formation of goethite. On annealing of goethite at 400 °C and above, hematite phase is formed. Scheme 1 shows the evolution and growth of as prepared and annealed particles.





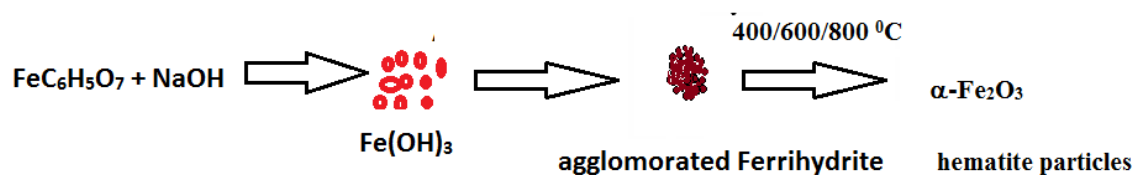
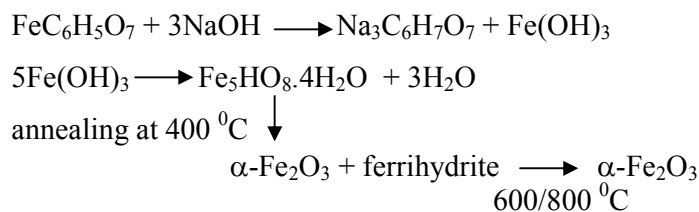
Scheme-1

Ferric nitrate-ammonia medium (sample K₂). Ammonia will form an unstable ferric ammine complex and hematite in ferric nitrate solution. The unstable complex will hydrolyze to give ferric hydroxide which will transform to ferrihydrite. With aging part of ferrihydrite will undergo dehydration and form goethite. Hence a mixture of ferrihydrite, hematite and goethite is formed. On annealing at 400 °C only hematite particles are formed which are spherical and elliptical in nature. Hematite particles form long chains consisting of several spherical nanoparticles for sample K₂ on annealing to 600 °C. On further annealing to 800 °C agglomeration and grain growth takes place which are presented in Scheme-2.



Scheme-2

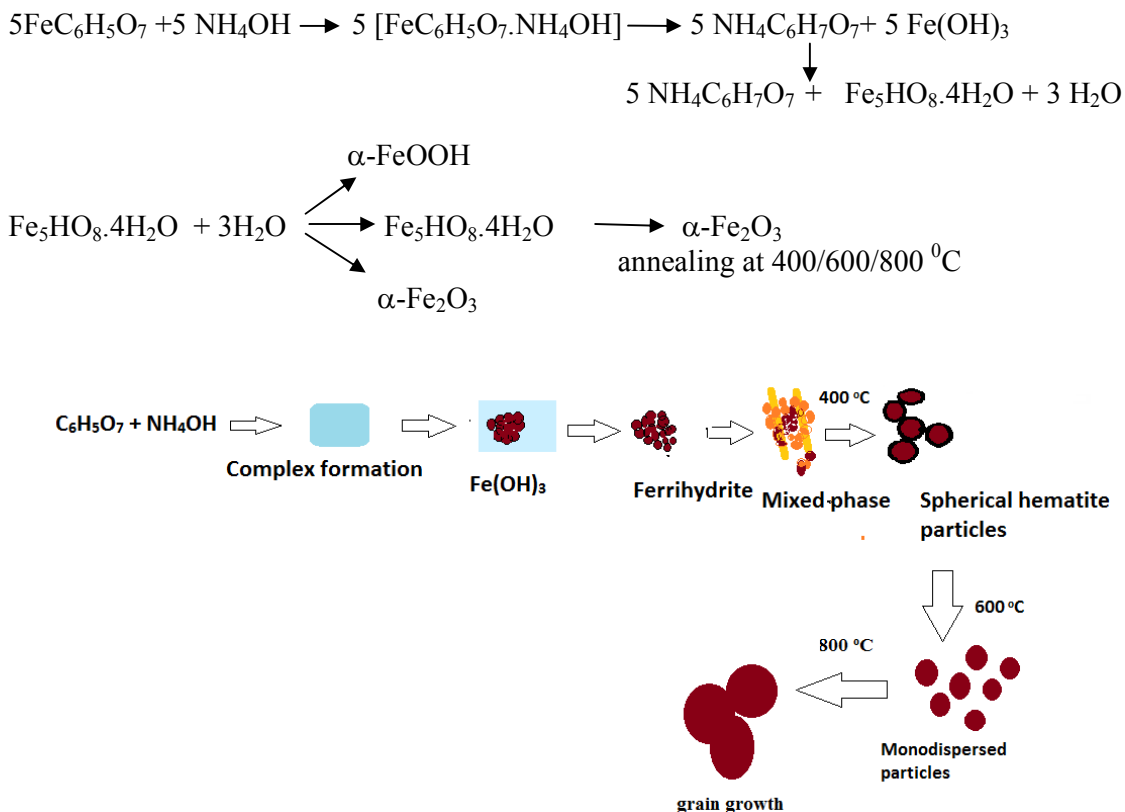
Ferric citrate-sodium hydroxide medium (sample K₃). In comparison to ferric nitrate-sodium hydroxide system, for ferric citrate-sodium hydroxide system very fine particles of ferrihydrite are formed. It is envisaged that the sodium citrate solution does not allow the phase transformation of ferrihydrite to goethite. On annealing at 400 °C mostly hematite with small amounts of ferrihydrite are observed. Further increase of annealing temperature to 600 or 800 °C results in the formation of pure hematite. The reactions taking place during precipitation and annealing are presented in Scheme-3.



Scheme-3

The formation of ferrihydrite seems to be slow so that no part of it is converted to goethite. In contrast when nitrate was used, during the aging itself, the ferrihydrite got converted into goethite.

Ferric citrate-ammonium hydroxide medium (sample K₄). When ferric citrate is used as the iron source and ammonium hydroxide as the neutralizing agent, first complex formation takes place followed by nucleation growth of ferric hydroxide followed by transformation of various phases. Ferrihydrite partly converts to goethite which undergoes dehydration to form hematite. Similar to ferric nitrate-ammonium hydroxide system in this case also the as prepared precursor is a mixture of ferrihydrite, goethite and hematite. A difference can be observed in % hematite formation. As per absorption areas quantified by Mössbauer data more goethite is formed and it has less of ferrihydrite content. On annealing at 400 °C near spherical hematite particles are formed which get monodispersed at 600 °C annealing temperature. Chemical reactions and mechanism are shown in Scheme-4.



Scheme-4

4. Conclusions

In the present studies it has been highlighted that by varying the starting reagents but keeping identical precipitation conditions single phased goethite, single phased ferrihydrite and mixed phases of ferrihydrite, goethite and hematite are evolved. When ammonia was used as the precipitating agent, irrespective of iron source, mixed phases containing goethite, ferrihydrite and hematite were formed. With sodium hydroxide as the precipitating agent single-phased goethite and single phased ferrihydrite were formed with ferric nitrate and ferric citrate respectively as the iron source. Annealing of the synthesized precursors in the range of 400 to 800 °C resulted in the formation of $\alpha\text{-Fe}_2\text{O}_3$ of different morphologies varying from rod like to spherical having different sizes. Detailed characterization studies of the as prepared and annealed samples carried out using XRD, TEM, Raman and Mossbauer spectroscopy have been presented. Raman spectra of annealed samples showed decrease/increase and the peaks were red/blue shifted with the increase in annealing temperature. The direct and indirect band gap energies for annealed samples estimated from

Uv-vis absorption spectra showed these values were dependent on the nature of phase present for as synthesized samples and on temperature of annealing for α -Fe₂O₃. For the annealed samples which were pure α -Fe₂O₃, the coercivity values changed from 29 to 2966 Oe. Probable mechanism during the chemical reaction has been included. The studies revealed the role of starting materials in iron oxides' phase formation, morphologies, optical and magnetic properties for the as synthesized and annealed samples.

AUTHOR INFORMATION

Corresponding Author

*Tel +91-674-2581635 extn. 9272; fax 864 656 5973; *mamatomohapatra [@yahoo.com](mailto:mamatomohapatra@yahoo.com)

Notes

The authors declare no competing financial interest.

Acknowledgement

The authors are thankful to Prof. B. K. Mishra, Director, Institute of Minerals and Materials Technology, Bhubaneswar, for his kind permission to publish this paper. One of the authors, K. Rout, is thankful to Council of Scientific and Industrial Research for providing her a senior research fellowship to carry out this work.

References

- 1 M. Tadic, V. Kusigerski, D. Markovic, M. Panjan, I. Milosevic, V. Spasojevic, *J. Alloys. Compd.*, 525, 2012, 28-33.
- 2 M. Mohapatra, S. Anand, *IJEST*, 2, 2010, 127-146.
- 3 P. Xu, G. M. Zeng, D. L. Huang, C. L. Feng, S. Hu, M. H. Zhao, C. Lai, Z. Wei, C. Huang, G. X. Xie, Z. F. Liu, *Sci. Total Environ.*, 424, 2012, 1-10.
- 4 C. Cannas, G. Concas, D. Gatteschi, A. Falqui, A. Musinu, G. Piccaluga, C. Sangregorio, G. Spano, *Phys. Chem. Chem. Phys.*, 3, 2001, 832-838.
- 5 U. Jeong, X. Teng, Y. Wang, H. Yang, Y. Xia, *Adv. Mater.*, 19, 2007, 33-60.
- 6 N. Pailhe, A. Wattiaux, M. Gaudon, A. Demourgues, *J. Solid State Chem.*, 181, 2008, 2697-2704.
- 7 T. Ninjbadgar, S. Yamamoto, T. Fukuda, *Solid State Sci.*, 6, 2004, 879-885.

- 8 G. A. Bukhtiyarova, M. A. Shuvaeva, O. A. Bayukov, S. S. Yakushkin, O. N. Martyanov, *J. Nanopart. Res.*, 13, 2011, 5527-5534.
- 9 Q. Wang, X. Yang, L. Yu, H. Yang, *J. Alloys Comp.*, 509, 2011, 9098-9104.
- 10 R. Zboril, M. Mashlan, D. Petridis, *Chem. Mater.*, 14, 2002, 969-982.
- 11 P. Li, D. E. Miser, S. Rabiei, R. T. Yadav, M. R. Hajaligol, *Appl. Catal. B-Environ.*, 43, 2003, 151-162.
- 12 N. D. Phu, D. T. Ngo, L. H. Hoang, N. H. Luong, N. Chau, N. H. Hai, *J. Phys. D: Appl. Phys.*, 44, 2011, 345002.
- 13 E. Darezereshki, *Mater. Lett.*, 65, 2011, 642-645.
- 14 C. E. Sjogren, C. Johansson, A. Naevestad, P. C. Sontum, K. BrileySaebo, *Magn. Reson. Imaging*, 15, 1997, 55-67.
- 15 J. P. Wilcoxon, P. P. Provencio, *J. Phys. Chem. B*, 103, 1999, 9809-9812.
- 16 C. T. Seip, C. Connor, *Nanostruct. Mater.*, 12, 1999, 183-186.
- 17 J. Van Wonterghem, S. Morup, *Phys Rev Lett*, 55, 1985, 410-413.
- 18 W. Q. Jiang, H. C. Yang, S. Y. Yang, H. E. Horng, J. C. Hung, Y.C. Chen, C. Y. Hong, *J. Magn. Mater.*, 283, 2004, 210-214.
- 19 S. L. Zhong, J. M. Song, S. Zhang, H. Yao, A. W. Xu, W. T. Yao, S. H. Yu, *J. Phys. Chem. C*, 112, 2008, 19916-19921.
- 20 X. Jia, L. Yang, H. Song, Y. Su, *Micro Nano Lett.*, 6, 2011, 806-808.
- 21 L. E. Davidson, S. Shaw, L. G. Benning, *Am. Mineral.*, 93, 2008, 1326-1337.
- 22 Z. An, J. Zhang, S. Pan, G. Song, *Powder Technol.*, 217, 2012, 274-280.
- 23 L. P. Zhu, H. M. Xiao, X. M. Liu, S. Y. Fu, *J. Mater. Chem.*, 16, 2006, 1794-1797.
- 24 Y. C. Zhang, J. Y. Tang, X. Y. Hu, *J. Alloy Compd.*, 462, 2008, 24-28.
- 25 X. Wang, *Mater. Res. Bull.*, 47, 2012, 2513-2517.
- 26 E. Darezereshki, F. Bakhtiari, M. Alizadeh, A. Behradvakylabad, M. Ranjbar, *Mater. Sci. Semicond. Process*, 15, 2012, 91-97.
- 27 B. Sun, J. Horvat, H. S. Kim, W-S Kim, J. Ahn, G. Wang, *J. Phys. Chem. C*, 114, 2010, 18753-18761
- 28 S. Chakrabarty, K. Chatterjee, *J. Cryst. Growth*, 381, 2013, 107-113.
- 29 J. Cai, S. Chen, M. Ji, J. Hu, Y. Ma, L. Qi, *Cryst. Eng. Comm.*, 16, 2014, 1553-1559.
- 30 H. Yang, X. Mao, Y. Guo, D. Wang, G. Ge, R. Yang, X. Qiu, Y. Yang, C. Wang, Y. Wang, G. Liu, *Cryst. Eng. Comm.*, 12, 2010, 1842-1849.

- 31 X-L Fang, C. Chen, M.-S. Jin, Q. Kuang, Z-X. Xie, S-Y. Xie, R-B. Huang, L-S. Zheng, *J. Mater. Chem.*, 2009, 19, 6154–6160.
- 32 Z. Pu, M. Cao, J. Y., K. Huang, C. Hu, *Nanotechnology*, 17, 2006, 799–804.
- 33 X. Gou, G. Wang, J. Park, H. Liu, J. Yang, *Nanotechnology*, 19, 2008, 125606 (7pp)
- 34 M. Kosmulski, S. Durand-Vidal, E. Maczka, J.B. Rosenholm, *J. Colloid Interface.Sci.*, 271 (2004) 261–269.
- 35 J.P. Gustafsson, Modelling molybdate and tungstate adsorption to ferrihydrite. *Chem. Geol.*, 200, 2003, 105-115.
- 36 Z. Li, T. Zhang, K. Li, *Dalton Trans*, 2011, 40, 2062-2066.
- 37 H. Liu, P. Li, B. Lu, Y. Wei, Y. Sun, *J. Solid State Chem.*, 182, 2009, 1767-1771.
- 38 A. I. Vogel, *A Text Book of Quantitative Inorganic Analysis*, English Language Book Society and Longmans Green Publishers, London, 2000.
- 39 M. Kosmulski, E. Maczka, E. Jartych, J. B. Rosenholm, *Adv. Colloid. Interf. Sci.*, 103, 2003, 57-76.
- 40 T. S. Berquo, J. J. Erbs, A. Lindquist, R. L. Penn, S. K. Banerjee, *J. Phys. Condens. Matter*, 21, 2009, 176005.
- 41 D. L. A. de Faria, S. Venâncio Silva, M. T. de Oliveira, *J. Raman Spectrosc.*, 28, 1997, 873-878.
- 42 C. Perez Leon, L. Kador, M. Zhang, A. H. E. Muller, *J. Raman Spectrosc.*, 35, 2004, 165-169.
- 43 K. Rout, M. Mohapatra, S. Anand, *Dalton Trans.*, 41, 2012, 3302-3312.
- 44 C. Y. Xu, P. X. Zhang, L. Yan, *J. Raman Spectrosc.*, 32, 2001, 862-865.
- 45 B. Santara, B. Pal, P.K. Giri, *J Appl Phys*, 110, 2011, 114322 (7pp).
- 46 M. J. Seepanovic, M. Grujic-Brojcin, Z. D. Dohcevic-Mitrovic, Z. V. Popovic, *Sci. Sinter.*, 41, 2009, 67-73.
- 47 C.A. Taylor, M. F. Wayne, W. K. S. Chiu, *Carbon*, 41, 2003, 1867-1875.
- 48 G. Sridharan, S. K. Narayandass, D. Mangalaraj, H. C. Lee, *J. Optoelectronics Adv. Mater.*, 7(3), 2005, 1483-1491.
- 49 D. Regonini, A. Jaroenworuluck, R. Stevens, C. R. Bowen, *Surf. Interface. Anal.*, 42, 2010, 139-144.
- 50 C.K. Chung, M.W. Liao, C.W. Lai, *Thin Solid Films*, 518, 2009, 1415-1418.
- 51 M. C. Mathpal, A. K. Tripathi, M. K. Singh, S. P. Gairola, S. N. Pandey, A. Agarwal, *Chem. Phy. Letts.*, 555, 2013, 182-186.

- 52 S. Xie, E. Iglesia, A. T. Bell, *J. Phys. Chem. B*, 105, 2001, 5144-5152.
- 53 J. Yang, X. Liu, L. Yang, Y. Wang, Y. Zhang, J. Lang, M. Gao, B. Feng, *J. Alloys Compd.*, 477, 2009, 632-635.
- 54 R. M. Cornell, U. Schwertmann, *The Iron Oxides*, 2nd ed., Wiley-VCH GmbH & Co. KGaA, Weinheim, Germany, 2003.
- 55 J. M. Combes, A. Manceau, G. Calas, Y. Bottero, *Geochim. Cosmochim. Acta.*, 53, 1989, 583-594.
- 56 A. C. Scheinost, A. Chavernas, V. Barron, Torrent, *J. Clays Clay Miner.*, 46, 1998, 528-536.
- 57 J. Tauc, *Mater. Res. Bull.*, 5, 1970, 721-729.
- 58 A. Duret, M. Gratzel, *J Phys Chem B*, 109, 2005, 17184-17191.
- 59 H. Zhang, M. Bayne, S. Fernando, B. Legg, M. Zhu, R. L. Penn, J. F. Banfield, *J. Phys. Chem. C*, 115, 2011, 17704-17710.
- 60 G. Liu, S. Debnath, K. Paul, W. Han, D. B. Hausner, H. A. Hosein, F. M. Michel, J. B. Parise, D. L. Sparks, D. R. Strongin, *Langmuir*, 22, 2006, 9313-9321.
- 61 Y. P. He, Y. M. Miao, C. R. Li, S. Q. Wang, L. Cao, S. S. Xie, G. Z. Yang, B. S. Zou, *Phys. Rev. B*, 71, 2005, 125411 (9 pp).
- 62 D. A. Wheeler, G. Wang, Y. Ling, Y. Li, J. Z. Zhang, *Energy Environ. Sci.*, 5, 2012, 6682-6702.
- 63 W.B. Ingler Jr., S. U. M. Khan, Photoresponse of p-Fe₂O₃ for water electrolysis under solar simulated light illumination, Department of Chemistry and Biochemistry Duquesne University, Pittsburgh, PA. 15282
- 64 N. J. Tharayil, R. Raveendran, A. V. Vaidyan, P.G. Mishra, *Ind. J. Eng. Mater. Sci.*, 15, 2008, 489-496.
- 65 A. Maurya, P. Chauhan, S. K. Mishra, R. K. Srivastava, *J. Alloys Compd.*, 509, 2011, 8433-8440.
- 66 R. S. Zergenyi, A. M. Hirt, S. Zimmermann, J. P. Dobson, W. Lowrie, *J. Geophys. Res.* 105, 2000, 8297-8303.
- 67 D.W. Strangway, R. M. Honea, B. E. McMahon, E. E. Larson, *Geophys. J. Royal Astronom. Soc.*, 15(4), 1968, 345-359.
- 68 C.G. Shull, W.A. Strauser, E.O. Wollan, *Phys. Rev.*, 83, 1951, 333-345.
- 69 F. J. Morin, *Phys. Rev.*, 78, 1950, 819-820.
- 70 S. Mitra, S. Das, K. Mandal, S. Chaudhuri, *Nanotechnology*, 18, 2007, 275608.

- 71 J. J. M. Abdul Khadar, *J. Magn. Magn. Mater.*, 322, 2010, 614-621.
- 72 J. Jacob, M. A. Khadar, *J. Magn. Magn. Mater.*, 322, 2010, 614-621.
- 73 K. K. Sahu, C. Rath, N. C. Mishra, S. Anand, R. P. Das, *J. Colloid Interface Sci.*, 185, 1997, 402-410.
- 74 L. Suber, P. Imperatori, A. Mari, G. Marchegiani, M. V. Mansilla, D. Fiorani, W. R. Plunkett, D. Rinaldi, C. Cannas, G. Ennas, D. Peddis, *Phys. Chem. Chem. Phys.*, 12, 2010, 6984-6989
- 75 C. Chang, C. Zhang, W. Wang, Q. Li, *Rare Met.*, 29, 2010, 501-504.
- 76 B. Vallina, J. D. Rodriguez-Blanco, A. P. Brown, L. G. Benning, J. A. Blanco, *J. Nanopart. Res.*, 16, 2014, 2322, 13 pages.
- 77 C. Rath, K. K. Sahu, S. D. Kulkarni, S. Anand, S. K. Date, R. P. Das, N. C. Mishra, *Appl. Phys. Lett.*, 75, 1999, 4171-4173.

Table 1. Coding of Samples Prepared Using Different Reagents

Sample Code	Fe source	neutralizing agent	pH
K ₁	Iron nitrate	NaOH	12
K ₂	Iron nitrate	NH ₃	12
K ₃	Iron citrate	NaOH	12
K ₄	Iron citrate	NH ₃	12

Table 2. Mössbauer Parameters I.E., Isomer Shift (IS), Quadruple Splitting (QS), Hyperfine Field (B_{HF}), Line Width (LWD) and Area Ratio of all the Samples Annealed at 400 °C, 600 °C and 800 °C.

Temp °C	Sample	IS (mm/s) (±0.02)	QS(mm/s) (±0.02)	LWD (mm/s) (±0.02)	B_{HF} (T) (±0.1)	Area (%) (±2)	Phase
400	K ₁	0.36	-0.19	0.32	51.2	100	Hematite
	K ₂	0.35	-0.20	0.33	51.1	100	Hematite
	K ₃	0.31	0.72	0.30		4	Ferrihydrite
		0.35	-0.19	0.35	51.2	67	Hematite
		0.35	-0.19	0.37	47.0	29	Hematite
K ₄	0.36	-0.20	0.33	51.6	100	Hematite	
600	K ₁	0.35	-0.19	0.27	51.5	100	Hematite
	K ₂	0.35	-0.19	0.32	51.5	100	Hematite
	K ₃	0.35	-0.19	0.36	51.4	100	Hematite
	K ₄	0.35	-0.20	0.29	51.5	100	Hematite
800	K ₁	0.35	-0.20	0.26	51.6	100	Hematite
	K ₂	0.35	-0.19	0.27	51.6	100	Hematite
	K ₃	0.35	-0.19	0.28	51.4	100	Hematite
	K ₄	0.35	-0.19	0.28	51.6	100	Hematite

Table 3. Direct And Indirect Band Gaps of As Synthesized and Annealed Samples

Samples	Band-gap (eV)	
	Direct	Indirect
K ₁ as synthesized	2.8	2.1
K ₂ as synthesized	2.1	1.7
K ₃ as synthesized	2.65	1.7
K ₄ as synthesized	1.9	1.2
K ₁ (400 °C)	1.5	1.2
K ₂ (400 °C)	1.6	1.4
K ₃ 400 °C	1.6	1.2
K ₄ 400 °C	1.4	1.1
K ₁ (600 °C)	1.4	1.1
K ₂ 600 °C	1.5	1.4
K ₃ 600 °C	1.4	1.1
K ₄ 600 °C	1.2	0.9
K ₁ (800 °C)	1.4	1.1
K ₂ 800 °C	1.4	1.3
K ₃ 800 °C	1.4	1.0
K ₄ 800 °C	1.2	0.9

Table 4. Magnetization at Highest Applied Magnetic Field (1.5T) ($M_{1.5T}$), Remanent Magnetization (M_r), Coercive Field (H_C) and Squareness (S) of all the Samples Measured at 300 K Using a Vibrating Sample Magnetometer.

Annealing Temp. ($^{\circ}\text{C}$)	Sample	$M_{1.5T}$ (emu/g)	M_r (emu/g)	H_C (Oe)	S= M_r/M_S
As-prepared	K ₁	0.481	0.001	26	0.002
	K ₂	5.415	0.007	15	0.001
	K ₃	3.80	0	0	0
	K ₄	3.842	0.016	47	0.004
400	K ₁	0.326	0.004	138	0.013
	K ₂	0.432	0.072	1917	0.166
	K ₃	1.182	0.004	29	0.003
	K ₄	0.522	0.077	1311	0.148
600	K ₁	0.383	0.004	1093	0.11
	K ₂	0.487	0.10	2021	0.204
	K ₃	0.368	0.025	759	0.068
	K ₄	0.499	0.100	1852	0.200
800	K ₁	0.471	0.084	1415	0.178
	K ₂	0.451	0.099	2966	0.220
	K ₃	0.386	0.095	307	0.246
	K ₄	0.429	0.076	1895	0.177

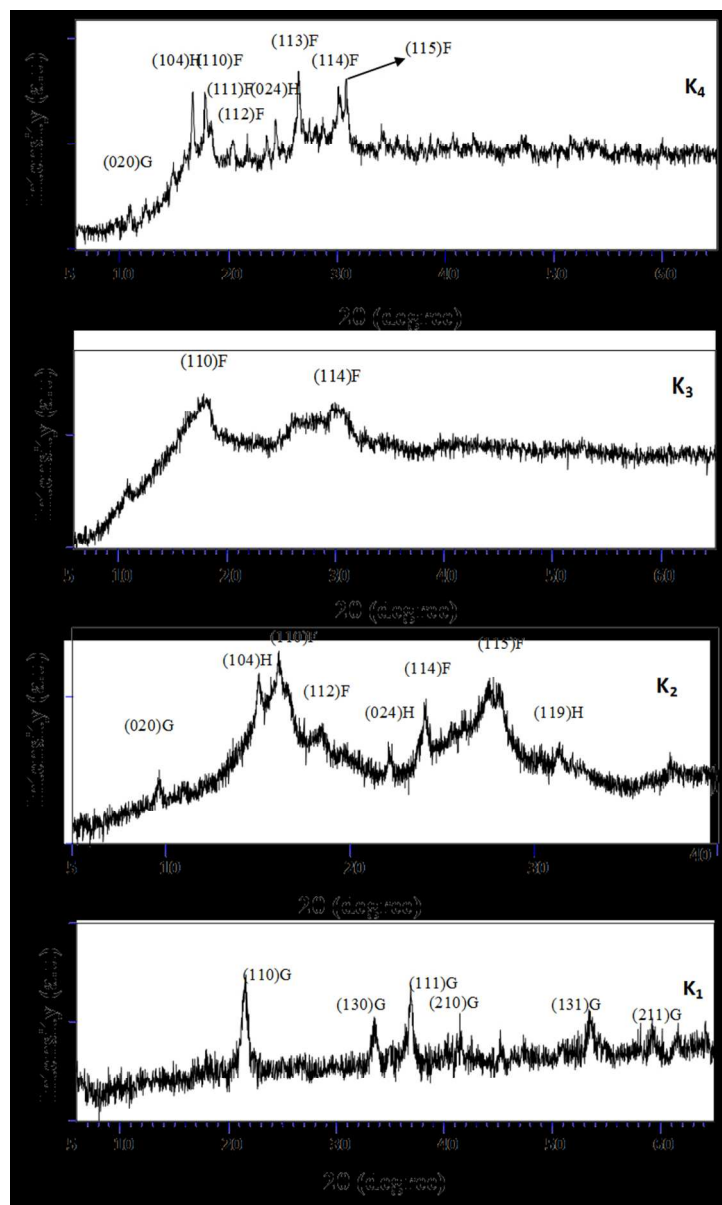


Figure 1. XRD pattern of as synthesised samples K1, K2, K3 and K4.
133x221mm (150 x 150 DPI)

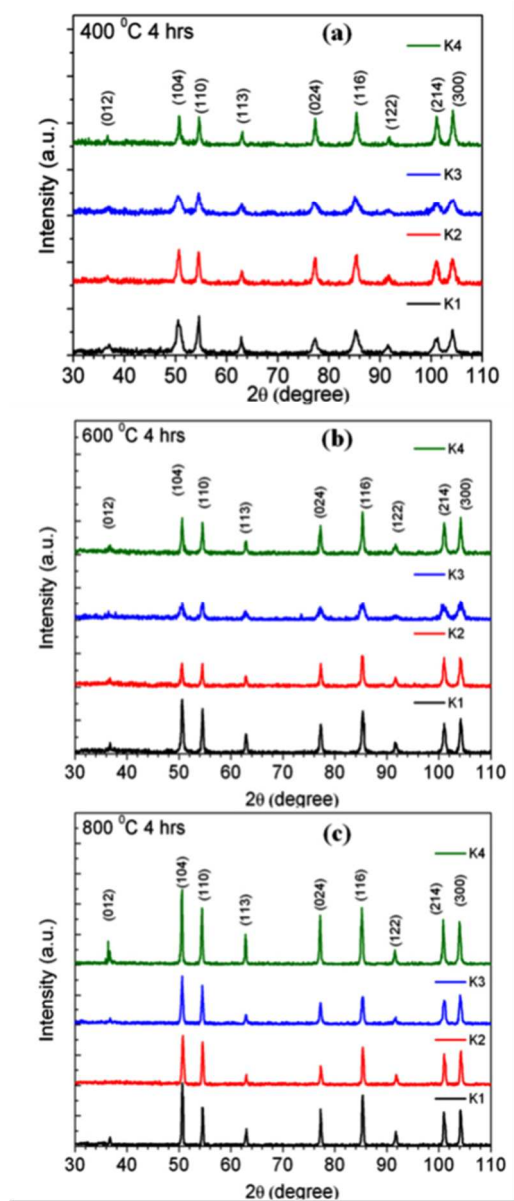


Figure 2. X-ray diffraction (XRD) patterns of samples annealed at (a) 400 °C, (b) 600 °C and, (c) 800 °C.
131x309mm (96 x 96 DPI)

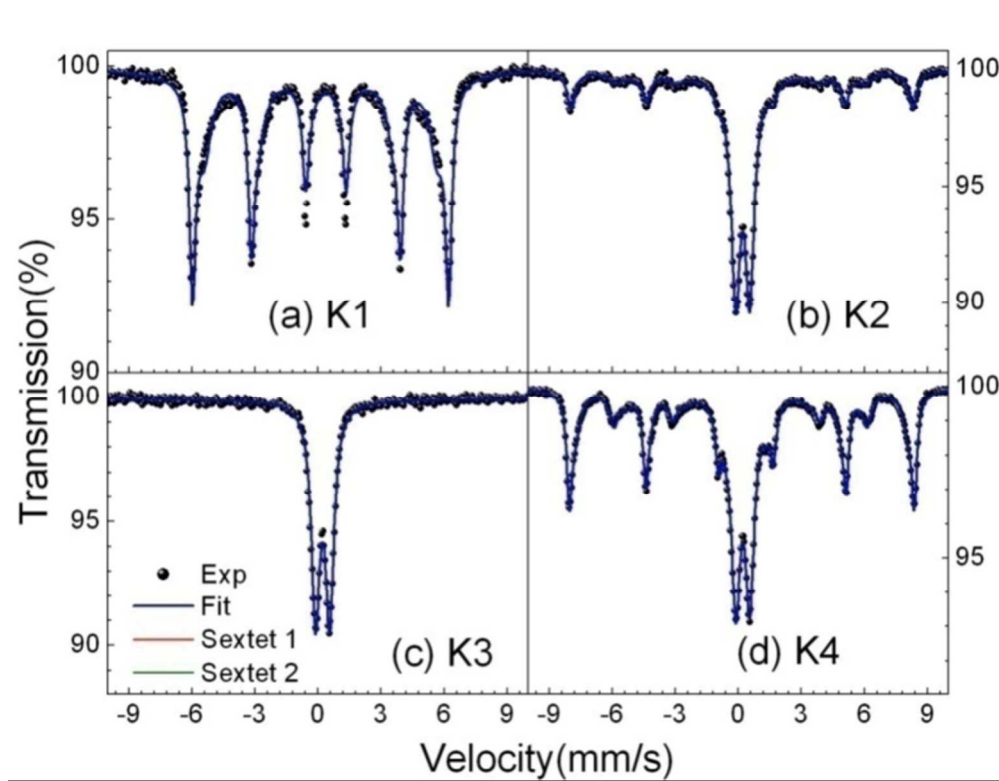


Figure 3. Mössbauer spectra of as-synthesized samples (a) K1, (b) K2, (c) K3 and (d) K4 recorded at 300 K.
186x143mm (300 x 300 DPI)

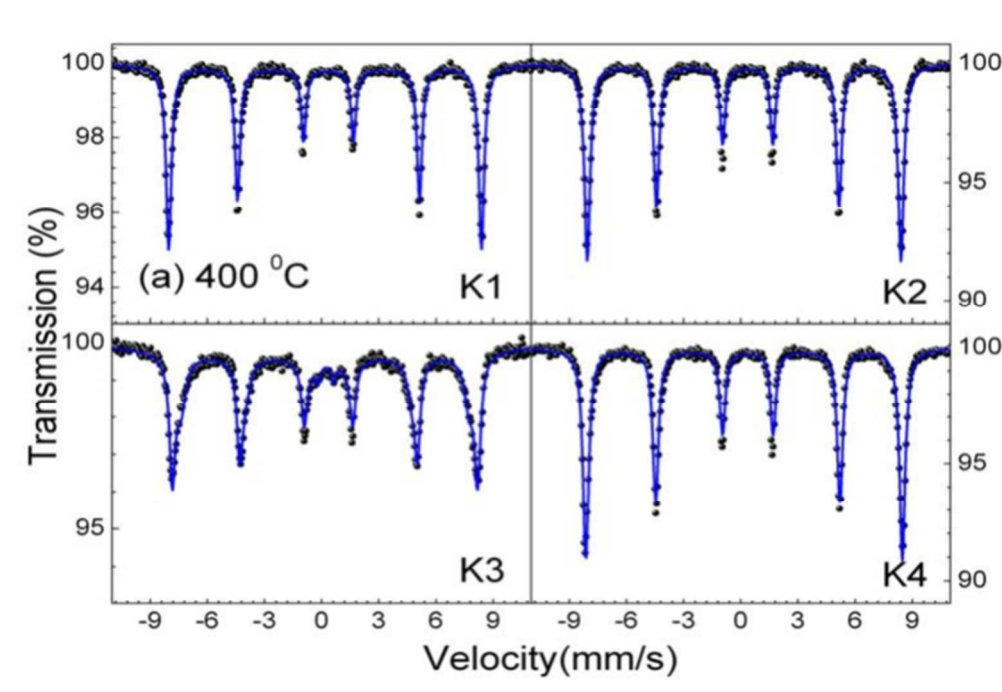


Figure 4. Mössbauer spectra of the K1, K2 K3 and K4 samples annealed at 400 °C recorded at 300 K.
140x96mm (300 x 300 DPI)

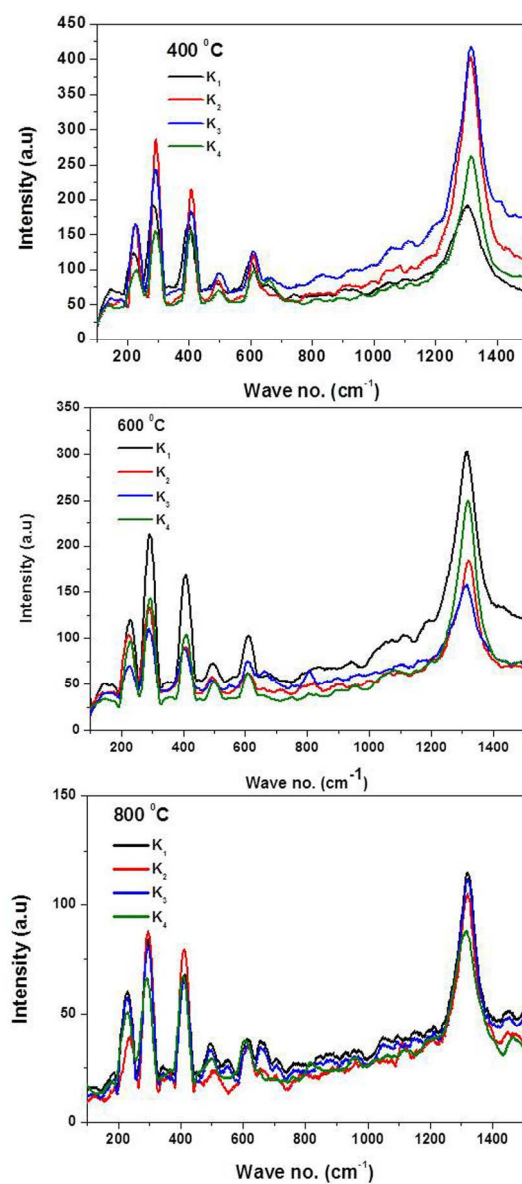


Figure 5. Comparison of Raman spectra of K1, K2, K3 and K4 samples annealed at (a) 400 °C, (b) 600 °C and, (c) 800 °C.

206x453mm (300 x 300 DPI)

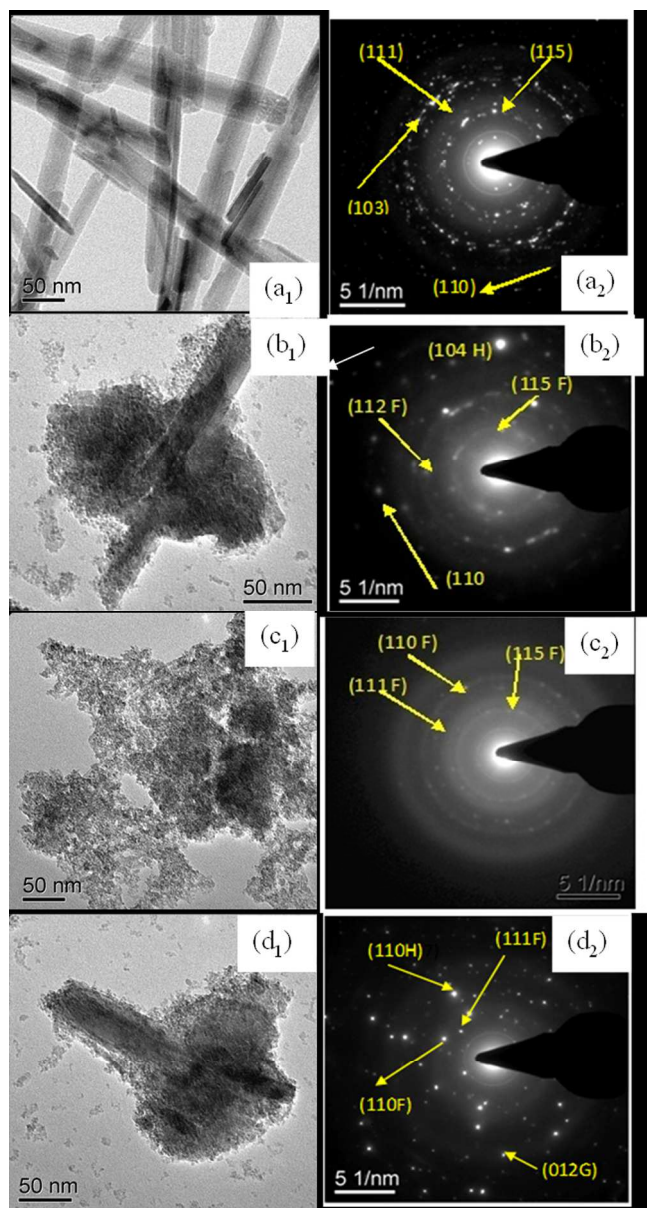


Figure 6. TEM images of sa synthesized samples (a1) K1, (a2) the corresponding SAED pattern, (b1) K2 (b2) the corresponding SAED pattern, (c1) K3, (c2) the corresponding SAED pattern, (d1) K4 , and (d2) the corresponding SAED pattern.

204x379mm (300 x 300 DPI)

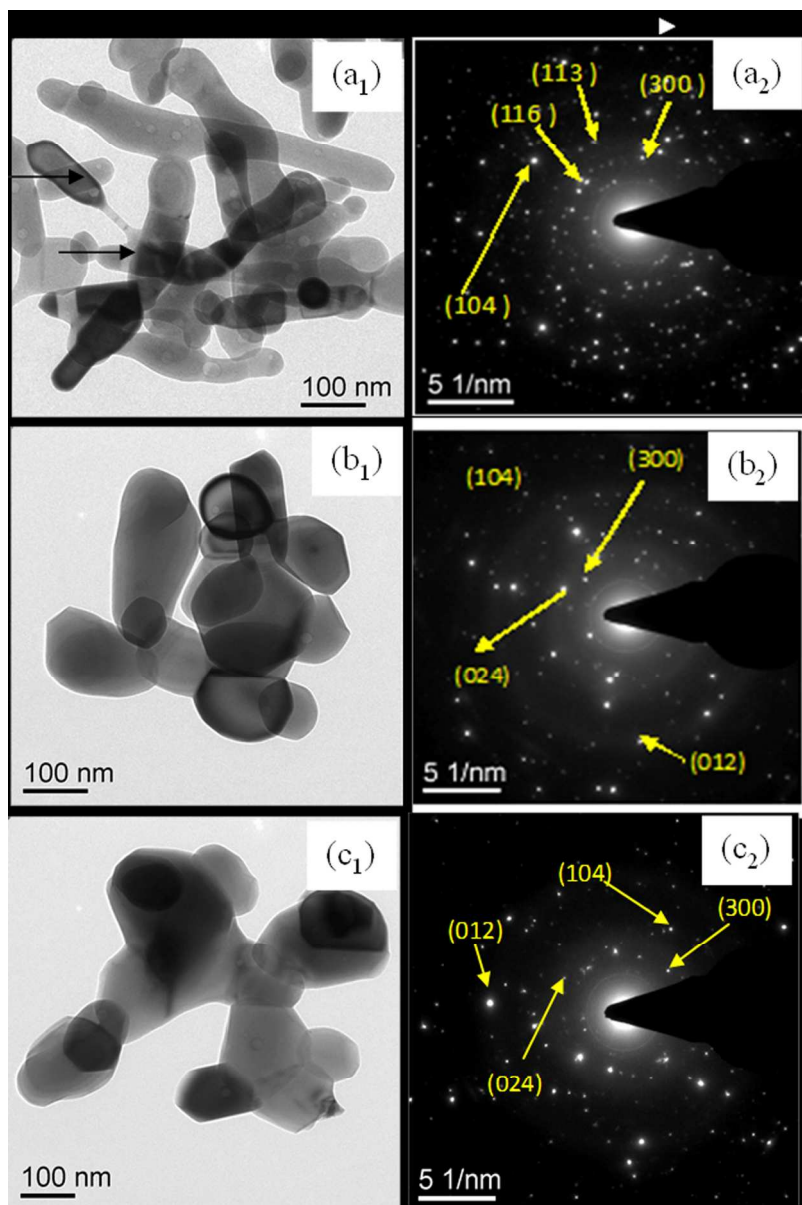


Figure 7. TEM image of K1 sample annealed at (a₁) 400 °C, (b₁) 600 °C and (c₁) 800 °C (a₂), (b₂) and (c₂) are the SAED patterns of K1 sample annealed at 400 °C, 600 °C and 800 °C respectively.

160x238mm (300 x 300 DPI)

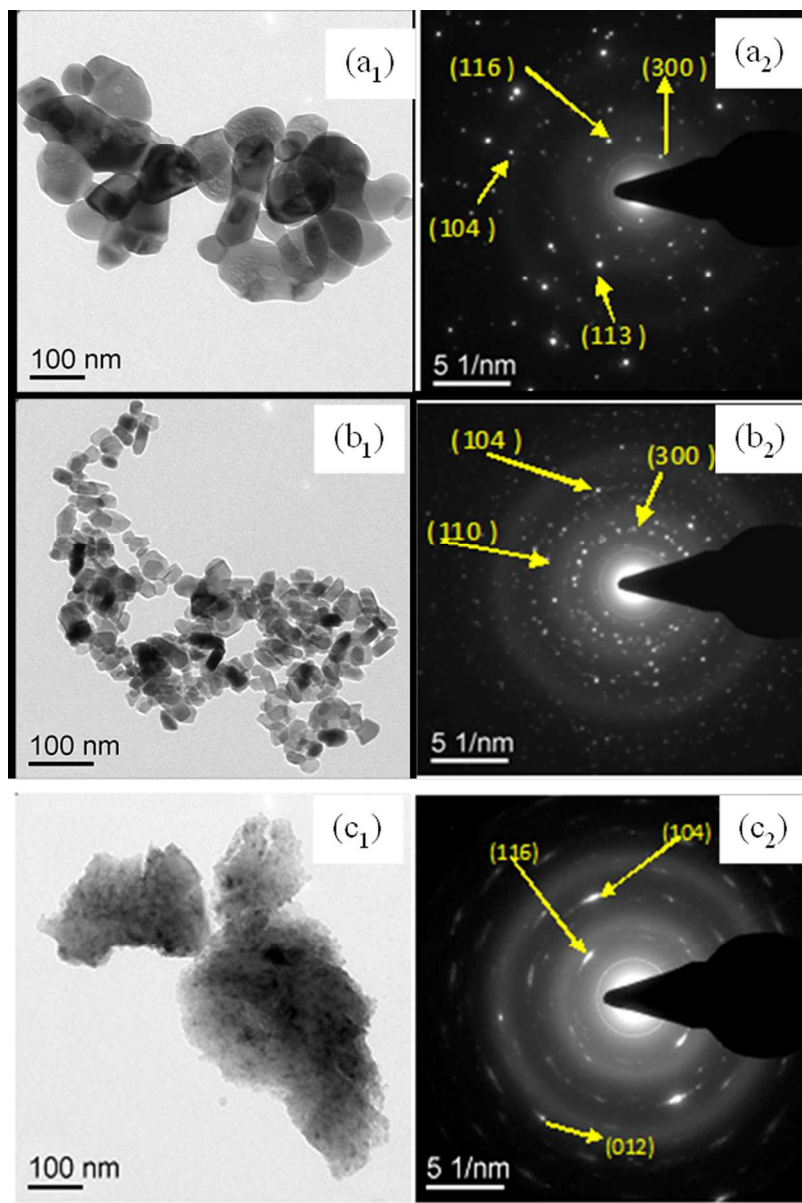


Figure 8. TEM image of K₂ sample annealed at (a₁) 400 °C, (b₁) 600 °C (c₁) 800 °C, (a₂), (b₂) and (c₂) are the corresponding SAED patterns of K₂ sample annealed at 400 °C, 600 °C and 800 °C.
159x237mm (300 x 300 DPI)

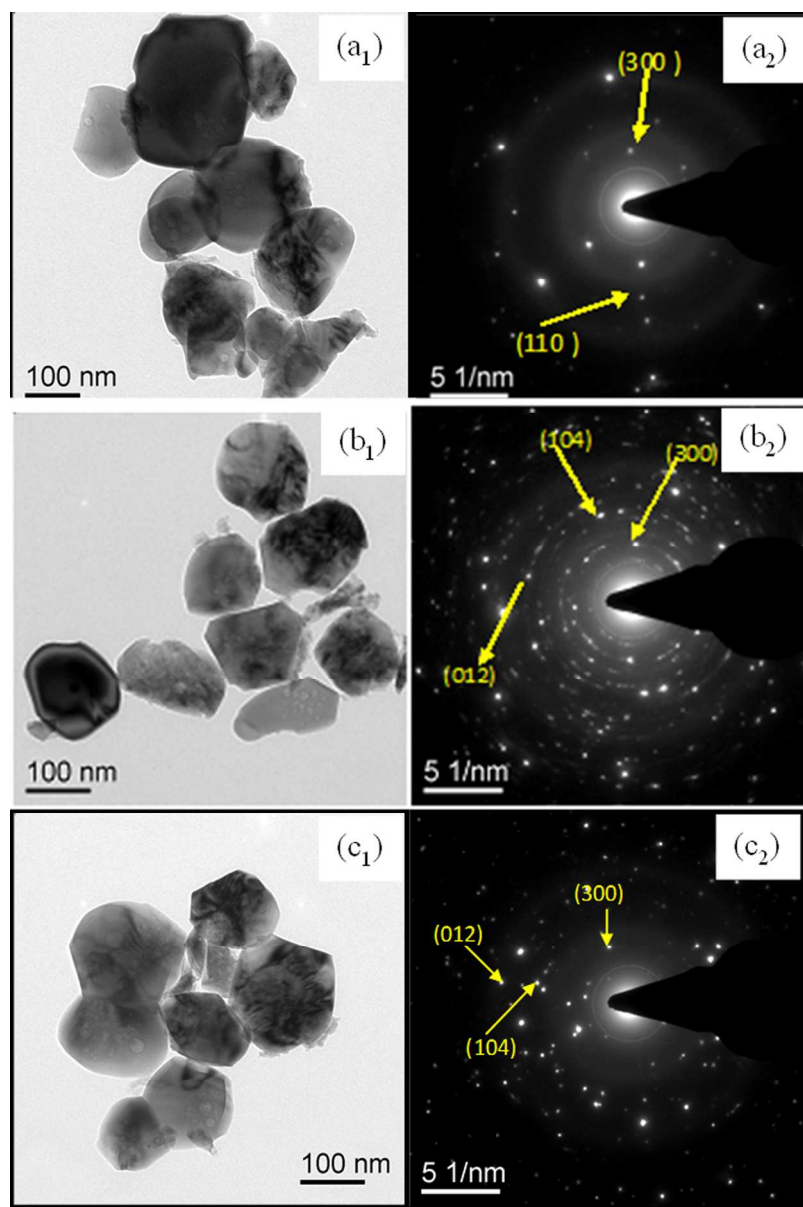


Figure 9. TEM image of K4 sample annealed at (a₁) 400, (b₁) 600 and (c₁) 800 °C. (a₂), (b₂) and (c₂) are the SAED patterns of K2 sample annealed at 400 °C, 600 °C and 800 °C respectively.

170x254mm (300 x 300 DPI)

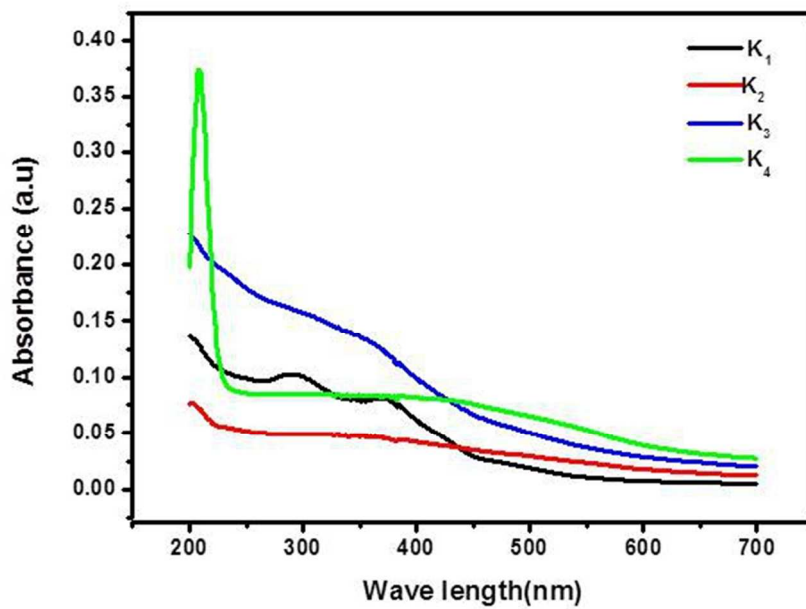


Figure 10. UV-Visible spectra of as synthesized K1, K2, K3 and K4 samples.
114x80mm (150 x 150 DPI)

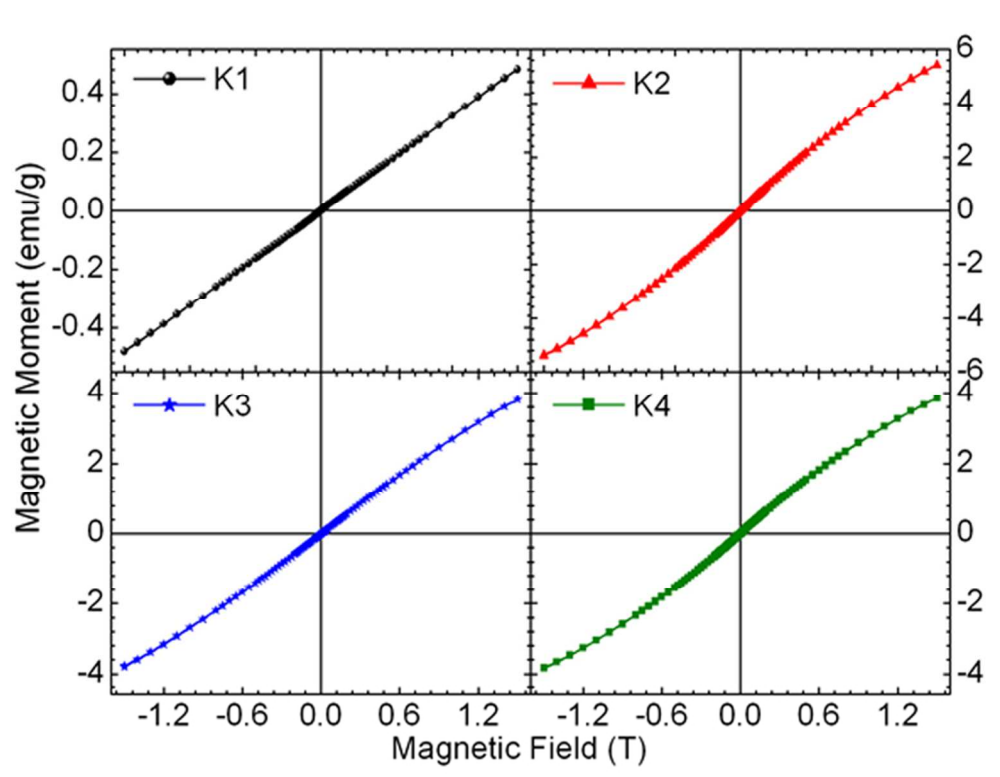


Figure 11. Magnetization as a function of applied magnetic field T (Tesla) for K1, K2, K3 and K4 as-synthesized samples recorded at 300 K.

77x59mm (300 x 300 DPI)

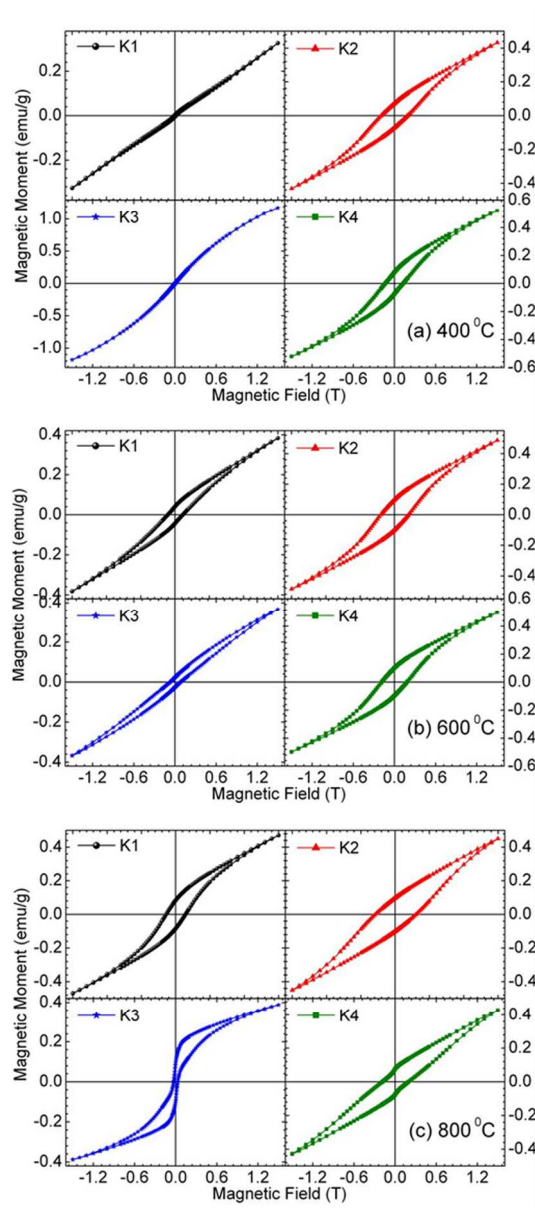


Figure 12. Magnetization as a function of applied field T (Tesla) for K1 , K2, K3 and K4 samples annealed at (a) 400 °C, (b) 600 °C and (c) 800 °C.

195x446mm (300 x 300 DPI)

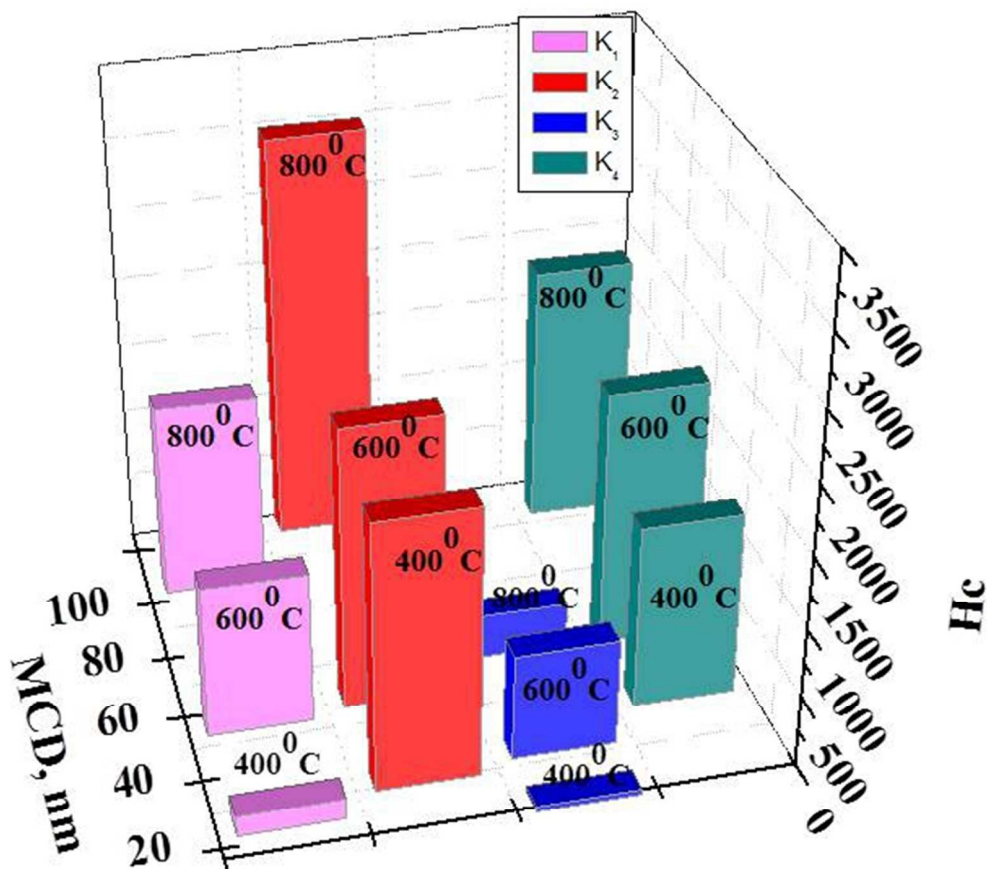


Figure 13. MCD (mean crystallite diameter as estimated from XRD data) vs. Hc (coercivity) for K1, K2, K3 and K4 samples annealed at 400, 600 and 800°C. (The experimental error in measuring magnetization for the present study is calculated to be 10^{-4} emu/g).

104x96mm (150 x 150 DPI)